1 **Title:** Sea floor bedforms and their influence on slope accommodation.

2

3 **Authors:** Maselli, V.[1,2], Kneller, B. [1], Taiwo, O.L. [1], Iacopini, D. [1]

4 [1]School of Geosciences, University of Aberdeen, Meston Bld., King's College, Aberdeen, AB24 3UF, United

5 Kingdom.

6 [2]Department of Earth Sciences, Life Sciences Centre, Dalhousie University, 1355 Oxford Street, Halifax, Nova

7 Scotia, B3H 4R2, Canada.

8

Keywords: Stoss accommodation space, intra-slope basin, turbidity currents, bedforms, offshore

10 Brazil.

11

12 **Highlights:**

13 1- 3D seismic data are used to investigate sea floor morphology and underneath stratigraphy

14 in the Potiguar Basin, offshore Brazil.

15 2- Large- and short-wavelength bedforms are recognized.

16 3- Ponded lobes accumulate on the stoss side of the large-wavelength bedforms, and seismic

17 attributes are used to characterize the associated lithology.

18 4- The concept of stoss accommodation space is introduced.

19

20 **Abstract**

21 In deep-water settings, the accommodation space for sediment transported by turbidity flows

22 relates to the difference between the elevation of the depositional surface and its equilibrium

23 profile. As a consequence, accommodation space creation, or disruption, may depend from

changes in the physiography of the receiving basin, or changes in the flow properties. In topographically complex slopes, such where salt-withdrawal intra-slope basins occur, three different types of accommodation space have been recognized. Among other parameters, the ratio between flow thickness and depth of the intra-slope basin controls the partial, or full, ponding of the sediment in suspension, and consequently, the lithology distribution within the deposit. On a smaller spatial scale, the behavior of turbidity flows is affected by the topography of the sea floor. Indeed, the presence of large-wavelength bedforms may generate local topographic low compared to the adjacent sea floor that may trap part of the sediment carried by sediment-laden flows, such as turbidity flows or bottom currents.

With a beautiful example from the offshore Brazil, we show how ponded lobes accumulate on the convex-up stoss side of pre-existing sea floor bedforms and how the three-dimensional topography of the sea floor controls the flow behavior and the deposition farther downslope. In detail, using 3D seismic data and attributes we demonstrate that the stoss side of the bedform traps the coarse-grained fraction of turbidity currents flowing downslope, while the fine-grained cloud spills over its crest. Further studies are necessary to fully understand the behavior of sediment-laden flows on a complex sea floor topography, the preservation potential of such deposits and the role of *stoss accommodation* in the evolution of deep-water depositional systems.

1. Introduction

Accommodation space was defined by Vail (1987) and Jervey (1988) as the space available for sediment accumulation, with global sea level change and tectonic processes (driving subsidence or uplift of the sea floor) considered as first order controls. In shallow water shelfal systems, the accommodation space available is also dependent from the energy of

2

48 marine processes, such as waves, longshore drift or tides, and by the presence of topographic

49 lows, such as incised valleys (Dalrymple et al., 1992).

50 In deep-water settings, the concept of accommodation space was expanded considering the

51 analogy between subaerial (rivers) and submarine channels, both characterized by

52 downstream concave-up equilibrium profiles and a base level (Carter, 1988; Prather et al.,

53 1998; Pirmez et al., 2000; Kneller, 2003). A topographic profile is considered in equilibrium,

54 or at grade, when the kinetic energy distribution along the system is such that no net sediment

55 aggradation or erosion occurs. In fluvio-deltaic systems the base level coincides with sea or

56 lake levels, i.e. the channel mouth, while for submarine channels the base level was defined

57 as the deepest point reached by a gravity-driven flow (Carter, 1988), or the point where the

58 transition from confined to unconfined flow occurs (Kneller, 2003). Turbidity currents exert a

59 paramount control on the shape of the equilibrium profile with the gradient of submarine

60 channels directly related to the flow conditions (flow density, thickness, grain size, mud

61 content; Mutti et al., 1999; Kneller, 2003). Considering the above, the accommodation space

62 was defined by the difference between the topography of the depositional surface (i.e., the

63 thalweg of a slope turbidite channel) and its equilibrium profile (Prather et al., 1998; Pirmez

64 et al., 2000). When a submarine channel is at grade, the accommodation space is limited, a

65 meandering planform morphology develops, with no aggradation or incision (Kneller, 2003),

66 producing fluvial-like meander belts (Abreu et al., 2003; Kolla et al., 2012).

67 A disequilibrium between the channel thalweg and the graded profile will lead to

68 accommodation space creation or destruction that the system will exploit through deposition

69 within the channel or erosion of its thalweg and rejuvenation of the system (Pirmez et al.,

70 2000; Heiniö and Davies, 2007). Several mechanisms, mainly driven by tectonic processes

71 (Prather et al., 1998; Pirmez et al., 2000; Ferry et al., 2005) or emplacement of mass-transport

72 deposits (Armitage et al., 2009; Kneller et al., 2016 and references therein), may lead to the

3

73 formation of accommodation space for sediment deposition. The topography of the slope may

74 change in response to shale or salt diapirism under loading by thick sediment accumulations,

75 or in response to gravitational tectonics driven by rapid sedimentation along passive margins

76 (Prather, 2003), or by crustal extension or compression, leading to the formation of ponded

77 and healed-slope accommodation space (*sensu* Prather et al., 1998). Ponded slope basins have

78 been recognized in different settings, both modern and ancient, and extensively investigated

79 in the Gulf of Mexico and in the Eastern Equatorial Atlantic margin (Prather et al., 1998;

80 Beaubouef and Friedmann, 2000; Pirmez et al., 2000; Sinclair and Tomasso, 2002; Booth et

81 al., 2003; Smith, 2004; Barton, 2012; Deptuck et al., 2012; Prather et al., 2012; Jobe et al.,

82 2015; Jobe et al., 2017; Hawie et al., 2018). Through integration of seismic and well data, the

83 motif of the sedimentary infill has been interpreted in terms of a process of fill-and-spill, i.e

84 filling of the mini-basin by ponded turbidites and associated deposits, and subsequent bypass

85 from the shallower mini-basin to the one downslope (Winker, 1996; Prather et al., 1998;

86 Badalini et al., 2000; Prather et al., 2012). Mass-transport deposits (MTDs), ubiquitously

87 recognized in all margin settings, have the potential to generate different styles of

88 accommodation space and to control deep-water sediment routing systems (Kneller et al.,

89 2016; Soutter et al., 2018). Sediment may accumulate along the evacuation zone of

90 submarine landslides or along the relative topographic lows generated atop the MTDs by the

91 presence of blocks, faults, folds and compaction (Kneller et al., 2016).

92 Local topographic changes of the sea floor (i.e., bedforms) have been observed on the slope

93 in association with the passage of gravity-driven flows such as turbidity currents, or of

94 bottom currents (Wynn and Stow, 2002; Smith et al., 2007; Piper and Normark, 2009;

95 Rebesco et al., 2014; Talling et al., 2015; Symons et al., 2016 and references therein).

96 Turbidity and bottom currents interacting with the sea floor may generate bedforms both

97 depositional (sediment waves), erosional (scours), or mixed, generated where both erosion

98   and deposition occurs (terminology *sensu* Symons et al., 2016). Bedforms of different shapes,

99   aspect ratio, direction of migration and grain size, from mud to gravel, have been recognized

100   in both confined and unconfined settings, such as shelfal systems (Berndt et al., 2006), pro-

101   delta slopes (Casalbore et al., 2017), channel axis (Paull et al., 2010; 2011), channel levees

102   (Normark et al., 2002), and channel-lobe transitions (Carvajal et al., 2017). After the seminal

103   work of Fildani et al. (2006) on the Monterey East Channel, increasing attention has been

104   dedicated to the study of bedforms, including those described as cyclic steps and their

105   associated supercritical flow regimes (i.e., densimetric Froude numbers >1). Cyclic steps and

106   antidunes have been increasingly recognized along delta fronts (Normandeau et al., 2016;

107   Hughes Clarke, 2016) and slope channel systems (Covault et al., 2017), and a growing body

108   of evidence has suggested that channels may evolve from a series of erosional bedforms

109   arranged in a cyclic manner (i.e., cyclic steps; Fildani et al., 2013; Covault et al., 2014). On

110   the sea floor, erosional bedforms, or those with an erosional component, may reach up to 10^3

111   m in length and width, and up to 10^2 m in height (Cartigny et al., 2011; Symons et al., 2016),

112   often showing circular to elliptical morphology, such as in the case of the Monterey East

113   channel (Fildani et al., 2006). With respect to the adjacent sea floor, the stoss side of such

114   bedforms constitutes an area of lower bathymetry, and consequently represent

115   accommodation space for sediment accumulation.

116   This study aims to understand the role of topographic lows generated by turbidity-current-

117   related bedforms (both erosional and depositional) in promoting slope accommodation space

118   and affecting sediment dispersal patterns and pathways. Using an example from the Brazilian

119   slope in the offshore Potiguar basin, we will demonstrate how the stoss side of large-

120   wavelength bedforms may act as a mini-basin where coarse-grained sediments transported by

121   turbidity currents may accumulate generating ponded lobes. Moreover, we will discuss how

122   the flow transformation of turbidity currents through flow stripping across the bedform-

123 related ponded mini-basin may affect the sedimentation pathways and related sea floor

124 topography of the slope farther downslope.

125

2. Study Area and Geological Setting

127 The present study focuses on a portion of the Brazilian slope just south of the Equator, in the

128 offshore Potiguar basin, in water depths between ca. 700 m and 1800 meters below mean sea

129 level (m bmsl; Fig. 1). The area is characterized by a ca. 60 km wide, low angle (0.04°), shelf,

130 and a steep slope, dipping towards NE at ca. 3.8°. Towards the basin, in deeper water, a series

131 of volcanic islands and structural highs develop, creating troughs that interrupt the continuity

132 of the slope (Fig. 1).

133 The Potiguar basin is a NE-trending aborted rift with ~6,000 m thick sedimentary infill,

134 structurally characterized by SW-NE-trending asymmetric grabens separated by internal

135 basement horsts (Matos, 2000; Jovane et al., 2016). The rifting process began in response to

136 continental breakup between the Borborema and Benin-Nigeria provinces during the South

137 Atlantic opening in the Early Cretaceous (Matos, 2000). Rift phase deposition during the

138 Aptian to Campanian, consisted of fluvial to shallow-marine transgressive sediments (Araripe

139 and Feijó, 1994). The drift phase, starting in the Campanian, is characterized by thermal

140 subsidence and deposition of fluvio-deltaic to deep-water clastic sediments, with the Neogene

141 mainly recording the onset and evolution of the submarine canyon systems still active today.

142

3. Data and Methods

144 The dataset from the Potiguar Basin used in the present study consists of a high-quality 3D

145 full stack, Kirchhoff time-migrated reflection seismic volume, covering about ~2000 km^2,

146 and acquired by PGS in 2009 (Fig. 1). The line spacing is 12.5 m in both in-line and cross-

147 line directions. The sample interval is 2 milliseconds (ms). The data are zero-phase migrated

148 and displayed with Society for Exploration Geologists (SEG) normal polarity, so that an

149 increase in acoustic impedance is represented by a blue-red-blue reflection loop. The

150 dominant frequency (F) of the section of interest (upper 250 ms below the seabed) ranges

151 between 40 and 75 Hz. Sound velocities of 1,500 ms^{-1} and 1,800-2,500 ms^{-1} have been

152 respectively assigned for sea water and for the investigated interval below the sea floor, with

153 the latter velocity obtained from the sonic log of well CES-112, located 2 km to the SE (see

154 Fig. 1; Conde et al., 2007). Using those end-member velocities and frequencies, we estimate

155 a vertical resolution (defined as tuning thickness, or limit of separability, as λ/4, λ being the

156 wavelength of the P wave) as 5 m at the sea floor and 6 to 15.5 m for the units below. Taking

157 into account the focusing effect of Kirchhoff migration (Brown, 2004), a radius Fresnel zone

158 (with a radius equal to velocity $V_{average}$/4F) of 5 m to 15.5 m can be reasonably expected, and

159 therefore a minimum diameter 10-31 m represents the limit of our interpretation analysis on a

160 horizon (*sensu* Brown, 2004). However our ability to recognize sea floor features in plan

161 view, defined as detectability or limit of visibility (Brown, 2004), can go below the tuning

162 thickness limit (Brown, 2004); while in the 3D migrated dataset, reflectors (e.g., peak to peak)

163 will be at least 5 m thick, and two reflecting point in horizontal space need to be around 5-15

164 m a part, when we are mapping the seafloor as a surface horizon, geological features on

165 considerably smaller scales can be detected and visualized with greater detail (Reijenstein et

166 al., 2011). Thus we can describe geological and sedimentary features or patterns smaller than

167 the tuning thickness, although our capacity to define volumes is limited by the tuning

168 thickness.

169 The bathymetry of the sea floor, presented at a 12.50 × 12.5 m of horizontal resolution (Fig.

170 2), was generated picking the first reflection from the 3D seismic data. Two other seismic

171 horizons, H1 and H2, were identified on 2D arbitrary lines extracted from the 3D seismic

7

172 volume, based on the seismic facies and reflector terminations. The structural map of each

173 seismic horizon is presented as surface gridded at a 12.5×12.5 m of horizontal resolution.

174 Seismic attributes have been calculated and extracted from the sea floor horizon and include

175 both amplitude-derived (root-mean-square, RMS) and time-derived (variance) values. While

176 the variance, which measures the similarity of consecutive waveforms over a given sampling

177 window (3×3 traces in the present study), is useful for imaging lateral discontinuities (Chen

178 and Sidney, 1997; Brown, 2004), the RMS amplitude, which represents the square root of the

179 arithmetic mean of the squares of the amplitudes within a defined window interval (3

180 instantaneous traces in the present study), is helpful for revealing coarse-grained facies (Rijks

181 and Jauffred, 1991; Chen and Sidney, 1997; Brown, 2004).

182

4. Results

4.1. Sea floor morphology

185 The sea floor shows two main canyon-channel systems, named C-1 and C-3 (Fig. 2) that are

186 located towards NW and SE corners of the dataset, respectively. The depth of both channels

187 changes from ca. 400 m to less than 200 downslope, while the thalweg presents an average

188 gradient of 2.7° and a sinuosity index of 1.158, for C-1, and a gradient of 3.8° and a sinuosity

189 index of 1.028, for C-3 (Fig. 2). A smaller channel, C-2, ca. 90 m deep, crosses the slope with

190 an average thalweg gradient of 4.15° and a sinuosity index of 1.031. The present study

191 focuses in the slope area comprised between C-2 and C-3 (confined by the red line in Fig. 2).

192 Two narrow channel incisions (C-A and C-B, Fig. 2), up to 60 m deep and oriented SW-NE,

193 form upstream of a topographic step (slope break) oriented approximately NS (dashed red

194 line in Fig. 2). Farther downslope, the sea floor presents a series of large-wavelength

195 bedforms (Fig. 3), named LB1 to LB4, which are clearly highlighted by the variance attribute

extracted from the sea floor horizon (Fig. 3 right, and Fig. 4). The bedform wavelength

changes from ca. 4 km (LB1, Fig. 5) to less than 1 km (LB4, Fig. 5), while the bedform

height from ca. 150 m (LB1, Fig. 5) to less than 50 m (LB4, Fig. 5). The crests of the

bedforms show a sinuous shape, with dominant downslope convexity (Fig. 3), and are

progressively shifted towards East moving downdip, following the maximum gradient of the

sea floor.

In a cross section on the sea floor, the bedforms are downslope asymmetric, with seaward

dipping (LB1 and LB2, Fig. 3 bottom) or sub-horizontal (LB3 and LB4) stoss sides, and up to

8° dipping lee sides. A series a small channels (named gutter-like channels), up to 15 m deep,

incise the lee sides of LB1 to LB4, and the area farther downslope.

On the sea floor, the stoss side of LB1, just downdip of the slope break at the mouth of C-A

and C-B, is characterized by two fields of short-wavelength bedforms (SB1a and SB1b, Fig.

3), both symmetric (section a-b in Fig. 6) and asymmetric (section c-d in Fig. 6), and with

sinuous crests (Fig. 6, right). Wavelengths and heights are, on average, 120 m and 8 m,

respectively (Fig. 5). A third train of bedforms (named SB2) with linear crests and ca. 5 m

wave heights is present on the lee side of LB3 (SB2 in Fig. 3; section e-f in Fig. 6). We are

confident that the spatial (vertical and horizontal) resolution of the sea floor generated by

picking the sea floor horizon on the 3D seismic dataset is high enough to visualize such

small-scale sea floor features. Seismic artefacts are present in the data, as indicated the

contour-parallel undulations highlighted by the slope map of Fig. 6, but they are

characterized by a totally different seismic footprint (see section g-h in Fig. 6), unrelated to

the bathymetry, with wave height and length extremely short, which will not have any effect

on the interpreted structures.

The RMS amplitude extraction map of the sea floor (Fig. 7) shows lobe-shaped areas

characterized by high RMS values on the stoss side of each large-wavelength bedform

221 (highlighted in orange in the B/W version of the RMS map in Fig. 7C). In detail, high RMS

222 values can be found where SB1a, SB1b and SB2 fields develop (named Lobe A, Lobe B and

223 Lobe D, respectively, Figs. 6, 7), on the stoss side of LB2 (Lobe C, Figs. 6, 7), of LB4 (Lobe

224 E, Figs. 6, 7), and of LB3 towards the northern flank of channel C-3 (Lobe F in Figs. 6, 7).

225 High RMS amplitude values also characterize the southern flank of C-2, while low values can

226 be detected along the lee side of all the large-wavelength bedforms (Fig. 7)

227

4.2. Seismic stratigraphy

229 The stratigraphy of the study area, and in particular of the lobe-shaped areas identified in the

230 RMS attribute map (Fig. 7), has been revealed using a combination of 2D arbitrary lines

231 extracted from the 3D seismic cube, surface maps of key stratigraphic horizons and thickness

232 maps (Figs. 8, 9).

233 Horizon H1, identified by a continuous positive reflection, is the first continuous horizon

234 below the sea floor, which can be traced in much of the study area (Figs. 8, 9B). The horizon

235 forms at the base of a series of lobe-to-lens-shaped deposits (named Lobe A to Lobe F, in

236 Figs. 7, 8, 9), whose tops correspond to the sea floor and show high RMS amplitude values.

237 In the same position, corresponding to the stoss side of the large-wavelength bedforms (Figs.

238 3, 7), the surface map of H1 shows a series of topographic depressions, triangular to circular

239 in shape, with progressively reducing size downslope (Fig. 9B). Thickness map of the unit

240 between the sea floor and horizon H1 (Fig. 9D) shows a series of sediment depocenters up to

241 65 m thick (Lobe A, Fig. 9D), whose internal seismic character is highlighted in Figure 8

242 (Lobes A, B, D and F, as examples). Each lobe shows a positive relief respect to the adjacent

243 sea floor, and is confined basinward by the topography generated by the large-wavelength

244 bedforms (Fig. 8). Lobe A, in detail, is the largest sediment depocenter, covering a surface

10

245   area of ca. 3.5 km^2 (Fig. 9D), and is composed by thick, high-amplitude, and wavy reflections

246   (seismic lines 1, 2 and 5 in Fig. 8). The sea floor reflection on top of Lobe A is also wavy

247   (Fig. 8), and corresponds to the short-wavelength bedform field SB1a visible on the sea floor

248   maps of Figures 3 and 6. Thickness map (Fig. 9D) highlights that Lobe A is made up of two

249   bodies, with the shallower backstepping with respect to the deeper (see seismic line 5 in Fig.

250   8). Lobe A accumulates on the stoss side of the large-wavelength bedform LB1, which is

251   confined by horizon H1 at its top and horizon H2 at its base (Figs. 8, 9E). Horizon H2 shows

252   an erosional character, as highlighted by several truncated reflections (see the black arrows in

253   Fig. 8), and can be traced over part of the study area (Fig. 9C). The topographic depression

254   generated by H2 is exploited by the accumulation of LB1, which is a 90 m thick, L shaped,

255   sediment body (Fig. 9E), made by continuous and low amplitude reflections, showing lateral

256   (see seismic lines 3 and 4 in Fig. 8) and upslope (see seismic line 5 in Fig. 8) migration of

257   progradation, and internal erosional surfaces (highlighted by black dashed lines in the seismic

258   profiles of Fig. 8). The deposition of the large-wavelength bedform LB1 visible on the sea

259   floor (Figs. 3, 4) creates the accommodation space for the accumulation of Lobe A and its

260   downslope confinement, as shown by Figure 9F. Similar geometric relations are observed for

261   each Lobe B to F, where the deposition of a lower unit bounded by an erosional surface (see

262   the red dashed lines in seismic lines 6 and 7 in Fig. 8, and line 8 in Fig. 9) causes the

263   generation of the large-wavelength bedforms and for the formation of accommodation space

264   along the slope. RMS amplitude extraction of the sea floor integrated with the seismic facies

265   in cross section highlight that each lobe has high RMS values and is made by high-amplitude

266   reflections (Fig. 7). By contrast, the units beneath, which crop out on the seafloor along the

267   lee side of the large-wavelength bedforms, present low RMS amplitude and mainly low

268   amplitude seismic reflections (Figs. 7, 8, 9). Consequently, we can infer that the lobes are

269   made by coarser-grained (probably sandy) sediment compared to the deposit beneath that are

11

270   responsible for the formation of the large-wavelength bedforms, which are probably muddier.

271   Correlation of horizon H2 with the other erosional surfaces occurring farther downslope is

272   not straightforward, which poses problem is the development of a conceptual model for

273   explaining their evolution. In the supplementary material we present two models which take

274   into account the effect of different processes and the possibility that the erosional surfaces

275   occurred synchronously to H2, or not.

276

5. Discussion

278   Topographically complex slopes (*sensu* Smith, 2004) occur when tectonic processes or

279   deformations of the sea floor driven by sediment loading on a mobile substrate crate

280   topographic lows or highs that can affect the path and behavior of gravity-driven flows

281   traveling downslope. In such contexts, different types of accommodation space may exist

282   (namely ponded, healed and slope accommodation; Prather et al., 1998), whose infill reflects

283   the effect of changing accommodation space through time (due to deposition), on the

284   behavior of gravity flows, and on the instability of the slope (Prather, 2003). Accommodation

285   space can be generated *a-priori*, and then filled by sediments, or can be increased by

286   sediment loading during basin infill, as in the case of salt withdrawal intra-slope basins

287   (Winker, 1996; Prather et al., 1998). It has been demonstrated that also sediment compaction

288   may significantly increase slope accommodation (Reynolds et al., 1991).

289   As sediment suspension in turbulent flows depends on bed shear stress, which is directly

290   related to flow velocity, 3D sea floor topography may control sediment deposition, erosion or

291   bypass through flow non-uniformity (Kneller and McCaffrey, 1995). Sea floor bedforms in

292   unconfined settings, normally generated by both erosional or depositional turbidity flows and

293   bottom currents (Rebesco et al., 2014; Symons et al., 2016 and references therein), may

294 create relative topographic lows (i.e., the convex-up stoss side of the bedform) where the

295 sediment transported by newly generated gravity flows may accumulate. Such lows can be up

296 to 10^2 m height and 10^3 m long, ca. an order of magnitude smaller, in both dimensions, than

297 the intra-slope basins in the Gulf of Mexico, and may act as an intra-slope mini-basin

298 generating what here we call *stoss accommodation*. In the study area, deposition from

299 unconfined flows or bottom currents was probably responsible for the creation of stoss

300 accommodation through the deposition of the large-wavelength bedforms (LB1 to LB4 in Fig.

301 3; see supplementary material). The ability of a turbidity current to flow across a

302 topographically complex slope, such as a salt withdrawal mini-basin or a large-wavelength

303 bedform, depends on the flow type (surging vs continuous; Lamb et al., 2004), the flow

304 thickness (Lane-Serff et al., 1995), the internal Froude number and the flow stratification

305 (Kneller and McCaffrey, 1999). Complete ponding of the flow occurs if the entire flow is

306 trapped within the topographic depression (Patacci et al., 2015, and references therein), and

307 sedimentation farther downslope is expected after its filling, partial or total, through a process

308 called fill-and-spill (Prather et al., 1998). If the depression is small enough compared to the

309 flow, the turbidity current may be able to surmount its downstream lip: the coarse-grained

310 part of the flow will accumulate within the topographic low while the fine-grained cloud will

311 be able to escape through a process called flow stripping (Piper and Normark, 1983).

312 Experimental results of Lane-Serff et al. (1995) demonstrated that a volume-limited flow (i.e.,

313 a surge-like turbidity current) may rise a topographic relief up to 5 times the flow thickness.

314 If we consider the case of one of the largest bedforms discovered so far on the modern sea

315 floor (i.e., the Monterey East channel which shows a maximum wave height of 220 m;

316 Fildani et al., 2006), all the incoming flows thicker than 44 m (with a supercritical regime, as

317 from Lane-Serff et al., 1995) will likely be able to generate overspill from the downstream lip

318 of the bedform. Of course this is an approximation based on Lane-Serff et al. (1995)

numerical results, as flow stratification (density and velocity) is also key in controlling the

maximum run-up height of a turbidity current (Kneller and McCaffrey, 1999; Kneller and

Buckee, 2000). Considering the example of the Monterey East channel as a conceptual end

member, we can argue that turbidity currents thicker than ca. 40 meters will be likely able to

overspill from any topographic depressions generated by pre-existing sea floor bedforms. In

such scenario, stoss accommodation will be mainly exploited by deposition of the coarser

part of the flow, while the fine-grained cloud of the turbidity current will be likely to

overspill, potentially creating sandy ponded lobes. This mechanism may affect sediment

deposition farther downslope, and the potential development of new sediment corridors.

Although with some limitations due to the lack of vertical resolution of the seismic data, this

conclusion is supported by the results of this study, which show high RMS amplitude values,

considered a proxy for coarse-grained sediment, on the stoss side of each large-wavelength

bedform (Fig. 7), and the presence of small channel incisions (named gutter-like channels)

along their lee sides, which will control deposition towards the basin. In addition, the short-

wavelength bedforms on Lobe A (SB1a, Figs. 3, 5) show crest directions perpendicular to the

local slope, probably reflecting deposition from turbidity currents radially spreading at the

mouth of channel C-A, on the flat surface generated after the infill of the stoss side of LB1.

Similar features have been observed in other context and liked to deposition from turbidity

currents (Normandeau et al., 2015). Turbidity currents are highly sensitive to changes in sea

floor topography, as divergence or convergence of the streamlines produces sediment

deposition or erosion/bypass, respectively (Kneller and McCaffrey, 1995). As in the case of

supra-MTD topography (Kneller et al., 2016), pre-existing bedforms may create a complex

sea floor topography that will undoubtedly have an effect on the turbidity currents (i.e.,

deposition, erosion, bypass) depending on the flow properties and direction (see Kneller et al.,

2016 for further discussion) with respect to the stoss accommodation space available. Further

344 work is needed to evaluate the flow behavior across pre-existing large-wavelength bedforms

345 and for turbidity currents unrelated with the deposition of the bedforms themselves, to

346 quantify the facies association of the ponded lobes through direct sediment sampling, and

347 their preservation potential. This may shed lights on defining the role of stoss accommodation

348 in hydrocarbon exploration and in the whole evolution of deep-water depositional systems.

349

6. Conclusion

351 Sea floor topography is a first order control on the flow behavior of turbidity currents flowing

352 down the slope of continental margins. Intra-slope basins are normally associated to large-

353 scale deformation of the sea floor, mainly promoted by salt or gravitational tectonics. With an

354 example from the offshore Brazil, here we show that smaller-scale topographic variations of

355 the sea floor associated with bedforms, may have a large effect on subsequent turbidity

356 currents and may promote the formation of coarse-grained ponded lobes. In detail, bedforms

357 characterized by convex-up stoss sides form topographic lows compared to the sea floor near-

358 by, generating stoss accommodation. Depending on the flow characteristics of newly sourced

359 turbidity currents, flow stripping or fill-and-spill may occur, in the first case promoting the

360 formation of sandy ponded lobes. The existence of a 3D topography may capture the coarse-

361 grained fractions of the flows in the relative lows while promoting the delivery of only the

362 fine-grained part downstream. Further studies are needed to understand the role of stoss

363 accommodation in the evolution of turbidity flows and associated deposits, and their

364 preservation potential in the stratigraphy of continental margins.

365

371

Figure captions

373

374   Figure 1

375   Top: Digital elevation model of the Equatorial Atlantic margin (data from GEBCO). Centre:

376   close-up on the Potiguar Basin in the offshore Brazil; white rectangle represents the full 3D

377   seismic data coverage, while the study area is highlighted in red; black and orange lines mark

378   the position of the bathymetric profiles presented below. Bottom: bathymetric profiles cross

379   the Ceará high and across an open slope setting.

380

381   Figure 2

382   Top: Bathymetric map with 75 m spaced contour lines; white lines oriented NW-SE are the

383   bathymetric profiles presented below, while the thick and continuous red line marks the study

384   area. Note the two large canyon-channel systems bordering the study area (named C-1 and C-

385   3) and the narrower incisional channel C-2. The thin dashed red line marks the slope break at

386   the mouth of incisions C-A and C-B. Bottom: Bathymetric profiles across section AB, CD,

387   EF and GH showing the change of channel depth of C-1, C-2 and C-3 with bathymetric depth;

388   note the position of the slope break in sections AB and CD.

389

390 Figure 3

391 A: Bathymetric map of the study area with 75 m spaced contour lines; the while continuous

392 line marks the position of the bathymetric profile IJ presented in C, while the white dashed

393 lines mark the crest of the large-wavelength bedforms, named LB1 to LB4; the red dashed

394 line marks the slope break at the mouth of C-A and C-B; note the gutter-like channels. B:

395 variance attribute map extracted from the sea floor horizon; note the short-wavelength

396 bedforms (SB1a, SB1b, SB2). C: the bathymetric profile IJ showing the large- and short-

397 wavelength bedforms (gray rectangle) shown in black; the sea floor gradient along the section

398 IJ shown in red, with highlighted the different bedform fields.

399

400 Figure 4

401 Variance attribute extracted from the sea floor and presented in a 3D view. The white dashed

402 lines mark the crest of the large-wavelength bedforms (LB1 to LB4), while the red dashed

403 line marks the slope break at the mouth of C-A and C-B. Note the gutter-like channels (Gc)

404 and the short-wavelength bedform SB2.

405

406 Figure 5

407 Wave length (in km) and wave height (m) of the different bedform fields recognized in this

408 study. The inset is a zoom of the left corner of the diagram to highlight bedforms SB1a, SB1b

409 and SB2.

410

411 Figure 6

412 Plan view of the sea floor slope map (left) and a close-up 3D of the stoss side of LB1 (right);

413 the red dashed line marks the slope break at the mouth of C-A and C-B; blue squares 1 and 2

414 highlight short-wavelength bedform fields SB1a and SB2 (zoom visible below), while the red

415 square is an example of seismic artefact. Bathymetric profiles across section ab and cd show

416 bedform styles on SB1, while profile ef shows the bedforms on SB2 (bedform's crests

417 pointed by the arrows). Profile gf highlights the seismic artefacts, almost invisible on a

418 bathymetric profile. All the bathymetric profiles are presented at the same scale.

419

420 Figure 7

421 A: Top view of the RMS attribute map extracted from the sea floor horizon; the white dashed

422 lines mark the crest of the large-wavelength bedforms (LB1 to LB4), while the red dashed

423 line marks the slope break. B: RMS amplitude map presented on a 3D view. Note that the

424 stoss side of the bedforms is repeatedly characterized by high RMS amplitude values (named

425 Lobe 1 to Lobe F), while the lee side by lower values. Note the gutter-like channels (Gc). C:

426 Grey-scale version of the RMS attribute map presented in A. This graphic solution is used to

427 better highlight the different features: lobes in orange, crests of the large-wavelength

428 bedforms in dashed white line, slope break in dashed red line.

429

430 Figure 8

431 2D arbitrary lines (see inset map for location) extracted from the 3D seismic cube, all

432 presented at the same scale. Lines 1 to 5 show Lobes A and B, and the internal stratigraphy of

433 the large-wavelength bedform LB1, while Lines 6 and 7 show Lobe D and F, respectively.

434 Horizon H2, highlighted in red (note the truncated reflections in sections 4 and 5, for

435 example), marks the base of bedform LB1. Internal reflections of LB1 are continuous and

low-amplitude (internal erosional surfaces marked by black dashed lines), and present an

437 oblique to upslope direction of migration as seen on the 3D data. Horizon H1, highlighted in

438 black, can be traced at the base of the all the Lobes, which present a positive relief on the sea

439 floor and, when visible, the internal reflections are wavy and high-amplitude. Note the short-

440 wavelength bedform fields on the sea floor reflection. Red dashed lines on seismic Lines 6

441 and 7 highlight the erosional surface at the base of the LB3 and LB4, in analogy with horizon

442 H2.

443

444 Figure 9

445 Top: Seismic line across the large-wavelength bedforms LB1 to LB4, with highlighted

446 horizon H2 (continuous red line), horizon H1 (black line), and other erosional surfaces (red

447 dashed lines); see trackline in A. Horizon H1 can be traced in much of the study area and

448 forms the base of the ponded Lobes A to F. A: Sea floor bathymetry. B: Structural map of

449 horizon H1. C: Structural map of horizon H2, which highlights the base of LB1. D: Thickness

450 map generated by the difference between the sea floor and horizon H1, which highlights the

451 ponded Lobes A to F. E: Thickness map generated by the difference between H1 and H2

452 horizons, which highlights the large-wavelength bedform LB1. F: Combined thickness maps

453 showing how Lobe A is confined basinward by LB1, filling the accommodation space

454 generated by the stoss side of LB1.

455

References

457 Abreu, V., Sullivan, M., Pirmez, C., Mohrig, D., 2003. Lateral accretion packages (LAPs): an

458   important reservoir element in deep-water sinuous channels. Marine and Petroleum

459   Geology 20, 631-648.

460 Adeogba, A.A, McHargue, T.R., Graham, S.A., 2005. Transient fan architecture and

461   depositional controls from near-surface 3-D seismic data, Niger delta continental

462   slope. AAPG Bulletin 89, 627-643.

463 Araripe, P.T., Feijó, F.J., 1994. Carta estratigráfica da Bacia Potiguar. Boletim De

464   Geociências Da Petrobras 8, 127-141.

465 Armitage, D.A., Romans, B.W., Covault, J.A., Graham, S.A., 2009. The influence of mass-

466   transport-deposit surface topography on the evolution of turbidite architecture: The

467   Sierra Contreras, Tres Pasos Formation (Cretaceous), southern Chile. Journal of

468   Sedimentary Research 79, 287-301.

469 Badalini, G., Kneller, B., Winker, C.D., 2000. Architecture and processes in the Late

470   Pleistocene Brazos-Trinity turbidite system, Gulf of Mexico Continental Slope.

471   GCSSEPM Foundation 20th Annual Research Conference, Deep-Water Reservoirs of

472   the World, 40-103.

473 Barton, M.D., 2012. Evolution of an Intra-Slope Apron, Offshore Niger Delta Slope: Impact

474   of Step Geometry on Apron Architecture. In: Prather, B.E., Deptuck, M.E., Mohrig,

475   D., van Hoorn, B., Wynn, R.B., (Eds.), Application of the Principles of Seismic

476   Geomorphology to Continental -Slope and Base-of-Slope Systems: Case Studies from

477   Seafloor and Near-Seafloor Analogues. SEPM Special Publication 99, pp. 181-197.

478 Beaubouef, R.T., Friedmann, S.J., 2000. High Resolution Seismic/Sequence Stratigraphic

479   Framework for the Evolution of Pleistocene Intra Slope Basins, Western Gulf of

480   Mexico: Depositional Models and Reservoir Analogs. Deep-Water Reservoirs of the

481   World, Gulf Coast SEPM, 40-60.

482   Berndt, C., Cattaneo, A., Szuman, M., Trincardi, F., Masson, D., 2006. Sedimentary

483   structures offshore Ortona, Adriatic Sea - Deformation or sediment waves? Marine

484   Geology 234, 261-270.

485   Booth, J.R., Dean, M.C., Duvernay, III, A.E., Styzen, M.J., 2003. Paleo-bathymetric controls

486   on the stratigraphic architecture and reservoir development of confined fans in the

487   Auger Basin: central Gulf of Mexico slope. Marine and Petroleum Geology 20, 563-

488   586.

489   Brown, A.R., 2004: Interpretation of three-dimensional seismic data, 5th edition. AAPG

490   Memoir 42, Tulsa, Oklahoma, pp. 514.

491   Casalbore, D., Ridente, D., Bosman, A., Chiocci, F.L., 2017. Depositional and erosional

492   bedforms in Late Pleistocene-Holocene pro-delta deposits of the Gulf of Patti

493   (southern Tyrrhenian margin, Italy). Marine Geology 385, 216-227.

494   Carter, R.M., 1988. The nature and evolution of deep-sea channel systems. Basin Research 1,

495   41-54.

496   Cartigny, M.J.B., Postma, G., van den Berg, J. H., Mastbergen, D.R., 2011. A comparative

497   study of sediment waves and cyclic steps based on geometries, internal structures and

498   numerical modeling. Marine Geology 280, 40-56.

499   Carvajal, C., Paull, C.K., Caress, D.W., Fildani, A., Lundsten, E., Anderson, K., Maier, K.L.,

500   Mcgann, M., Gwiazda, R., Herguera, J.C., 2017. Unraveling the channel-lobe

501   transition zone with high-resolution AUV bathymetry: Navy Fan, Offshore Baja

502   California, Mexico. Journal of Sedimentary Research 87, 1049-1059.

503   Chen, Q., Sidney, S., 1997. Seismic attribute technology for reservoir forecasting and

504   monitoring. The Leading Edge 16, 445-448.

505 Condé, V.C., Lana, C.C., Pessoa Neto, O.C., Roesner, E.H., Morais Neto, J.M., Dutra, D.C.,
506   2007. Baciado Ceará. Bol. Geoc. Petrobras 15, 347-355.

507 Covault, J.A., Kostic, S., Paull, C.K., Ryan, H.F., Fildani, A., 2014. Submarine channel
508   initiation, filling and maintenance from sea-floor geomorphology and
509   morphodynamic modelling of cyclic steps. Sedimentology 61, 1031-1054.

510 Covault, J.A., Kostic, S., Paull, C.K., Sylvester, Z., Fildani, A., 2017. Cyclic steps and related
511   supercritical bedforms: Building blocks of deep-water depositional systems, western
512   North America. Marine Geology 393, 4-20.

513 Dalrymple, R.W., Zaitlin, B.A., Boyd, R., 1992. Estuarine facies models: conceptual basis
514   and stratigraphic implications. Journal of Sedimentary Petrology 62, 1130-1146.

515 Deptuck, M.E., Sylvester, Z., O'Byrne, C.J. Pleistocene seascape evolution above a "simple"
516   stepped slope-western Niger Delta. In: Prather, B.E., Deptuck, M.E., Mohrig, D., van
517   Hoorn, B., Wynn, R.B., (Eds.), Application of the Principles of Seismic
518   Geomorphology to Continental -Slope and Base-of-Slope Systems: Case Studies from
519   Seafloor and Near-Seafloor Analogues. SEPM Special Publication 99, pp. 199-222.

520 Ferry, J.N., Mulder, T., Parize, O., Raillard, S., 2005. Concept of equilibrium profile in deep-
521   water turbidite system: effects of local physiographic changes on the nature of
522   sedimentary process and the geometries of deposits. In: Hodgson, D.M., Flint, S.S.,
523   (Eds.), Submarine Slope Systems: Processes and Products, Geological Society of
524   London, Special Publications 244, pp. 181-193.

525 Fildani, A., Normark, W.R., Kostic, S., Parker, G., 2006. Channel formation by flow
526   stripping: large-scale scour features along the Monterey East Channel and their
527   relation to sediment waves. Sedimentology 53, 1265-1287.

528 Fildani, A., Hubbard, S.M., Covault, J.A., Maier, K.L., Romans, B.W., Traer, M., Rowland,

529   J.C., 2013. Erosion at inception of deep-sea channels. Marine and Petroleum Geology

530   41, 48-61.

531 Hawie, N., Covault, J.A., Dunlap, D., Sylvester, Z., 2018. Slope-fan depositional architecture

532   from high-resolution forward stratigraphic models. Marine and Petroleum Geology 91,

533   576-585.

534 Heiniö, P., Davies, R.J., 2007. Knickpoint migration in submarine channels in response to

535   fold growth, western Niger Delta. Marine and Petroleum Geology 24, 434-449.

536 Hughes Clarke, J.E., 2016. First wide-angle view of channelized turbidity currents links

537   migrating cyclic steps to flow characteristics. Nature Communications 7, 1-13.

538 Jervey, MT., 1988. Quantitative geological modeling of siliciclastic rock sequences and their

539   seismic expression. In: Wilgus, C.K., Hasting, B.S., Kendall, C.G.S.C., Posamentier,

540   H.W., Ross, C.A., Van Wagoner, J., (Eds.), Sea-level Changes-an Integrated

541   Approach, 42, SEPM Special Publication, pp. 47-69.

542 Jobe, Z.R., Sylvester, Z., Parker, A.O., Howes, N., Slowey, N., Pirmez, C., 2015. Rapid

543   adjustment of submarine channel architecture to changes in sediment supply. Journal

544   of Sedimentary Research 85, 729-753.

545 Jobe, Z.R., Sylvester, Z., Howes, N., Pirmez, C., Parker, A.O., Cantelli, A., 2017. High-

546   resolution, millennial-scale patterns of bed compensation on a sand-rich intraslope

547   submarine fan, western Niger Delta slope. Geol. Soc. Am. Bull. 129, 23-37.

548 Jovane, L., Figueiredo, J.J.P., Alves, D.V.P., Iacopini, D., Giorgioni, M., Vannucchi, P.,

549   Moura, D.S., Bezerra, F.H.R., Vital, H., Rios, I.L.A., Molina, E.C., 2016.

550   Seismostratigraphy of the Ceará Plateau: Clues to Decipher the Cenozoic Evolution of

551   Brazilian Equatorial Margin. Frontiers in Earth Science doi:10.3389/feart.2016.00090.

552   Kneller, B., McCaffrey, W.D., 1995. Modelling the effects of salt-induced topography on

553   deposition from turbidity currents. GCSSEPM Foundation 16th Annual Research

554   Conference Salt, Sediment and Hydrocarbons, 137-145.

555   Kneller, B., McCaffrey, W.D., 1999. Depositional effects of flow nonuniformity and

556   stratification within turbidity currents approaching a bounding slope: deflection,

557   reflection, and facies variation. Journal of Sedimentary Research 69, 980-991.

558   Kneller, B., Buckee, C., 2000. The structure and fluid mechanics of turbidity currents: a

559   review of some recent studies and their geological implications. Sedimentology, 47,

560   62-94.

561   Kneller, B., 2003. The influence of flow parameters on turbidite slope channel architecture.

562   Marine and Petroleum Geology 20, 901-910.

563   Kneller, B., Dykstra, M., Fairweather, L., Milana, J.P., 2016. Mass-transport and slope

564   accommodation: Implications for turbidite sandstone reservoirs. AAPG Bulletin 100,

565   213-235.

566   Kolla, V., Bandyopadhyay, A., Gupta, P., Mukherjee, B., Ramana, D.V., 2012. Morphology

567   and internal structure of a recent upper Bengal fan-valley complex. In: Prather, B.E.,

568   Deptuck, M.E., Mohrig, D., Van Horn, B., Wynn, R.B., (Eds.), Application of the

569   Principles of Seismic Geomorphology to Continental-Slope and Base-of-Slope

570   Systems: Case Studies from Seafloor and Near-Seafloor Analogues, SEPM, Special

571   Publication 99, pp. 347-369.

572   Lamb, M.P., Hickson, J.G., Marr, B., Sheets, B., Paola, C., Parker, G., 2004. Surging and

573   continuous turbidity currents: Flow dynamics and deposits in an experimental

574   intraslope minibasin. Journal of Sedimentary Research 74, 148-155.

575 Lane-Serff, G.F., Beal, L.M., Hadfield, T.D., 1995. Gravity current flow over obstacles.

576   Journal of Fluid Mechanics 292, 39-53.

577 Matos, R.M.D., 2000. Tectonic evolution of the Equatorial South Atlantic. In: Mohriak, W.U.,

578   Talwani, M.. (Eds.), Atlantic Rifts and continental margins, Geophysical Monograph,

579   115, Amreican Geophysical Union, pp. 332-354.

580 Mutti, E., Tinterri, R., Remacha, E., Mavilla, N., Angella, S., Fava, L., 1999. An introduction

581   to the analysis of ancient turbidite basins from an outcrop perspective AAPG Course

582   Note 39, pp. 93.

583 Normandeau, A., Lajeunesse, P., St-Onge, G., 2015. Submarine canyons and channels in the

584   Lower St. Lawrence Estuary (Eastern Canada): Morphology, classification and recent

585   sediment dynamics. Geomorphology 241, 1-18.

586 Normandeau, A., Lajeunesse, P., Poiré, A.G., Francus, P., 2016. Morphological expression of

587   bedforms formed by supercritical sediment density flows on four fjord-lake deltas of

588   the south-eastern Canadian Shield (Eastern Canada). Sedimentology 63, 2106-2129.

589 Normark, W.R., Piper, D.J.W., Posamentier, H., Pirmez, C., Migeon, S., 2002. Variability in

590   form and growth of sediment waves on turbidite channel levees. Marine Geology 192,

591   23-58.

592 Paull, C.K., Ussler III, W., Caress, D.W., Lundsten, E., Covault, J.A., Maier, K.L., Xu, J. and

593   Augenstein, S., 2010. Origins of large crescent-shaped bedforms within the axial

594   channel of Monterey Canyon, offshore California. Geosphere 6, 755-774.

595 Paull, C.K., Caress, D.W., Ussler III, W., Lundsten, E., Meiner-Johnson, M., 2011. High-

596   resolution bathymetry of the axial channels within Monterey and Soquel submarine

597   canyons, offshore central California. Geophere 7, 1077-1101.

598   Patacci, M., Haughton, P.D.W., McCaffrey, W.D., 2015. Flow behavior of ponded turbidity

599   currents. Journal of Sedimentary Research 85, 885-902.

600   Piper, D.J.W., Normark, W.R., 1983. Turbidite depositional patterns and flow characteristics,

601   Navy submarine fan, California Borderland. Sedimentology 30, 681-694.

602   Piper, D.J.W., Normark, W.R., 2009. Processes that initiate turbidity currents and their

603   influence on turbidites: a marine geology perspective. Journal of Sedimentary

604   Research 79, 347-362.

605   Pirmez, C., Beauboeuf, R.T., Friedmann, S.J., Mohrig, D.C., 2000. Equilibrium profile and

606   baselevel in submarine channels: examples from Late Pleistocene systems and

607   implications for the architecture of deepwater reservoirs. In: Weimer, P., Slatt, R.M.,

608   Coleman, J., Rosen, N.C., Nelson, H., Bouma, A.H., Styzen, M.J., Lawrence, D.T.,

609   (Eds.), Deep water reservoirs of the world, GCSSEPM Foundation, Houston (2000),

610   pp. 782-805.

611   Prather, B.E., Booth, J.E., Steffens, G.S., Craig, P.A., 1998. Classification, lithologic

612   calibration, and stratigraphic succession of seismic facies of intraslope basins, deep-

613   water Gulf of Mexico. American Association of Petroleum Geologists Bulletin 82,

614   701-728.

615   Prather, B.E., 2003. Controls on reservoir distribution, architecture and stratigraphic trapping

616   in slope settings. Marine and Petroleum Geology 20, 529-545.

617   Prather, B.E., Pirmez, C., Winker, C.D. 2012. Stratigraphy of linked intraslope basins:

618   Brazos-Trinity system Western Gulf of Mexico. In: Prather, B.E., Deptuck, M.E.,

619   Mohrig, D., van Hoorn, B., Wynn, R.B. (Eds.), Application of the Principles of

620   Seismic Geomorphology to Continental -Slope and Base-of-Slope Systems: Case

621   Studies from Seafloor and Near-Seafloor Analogues. SEPM Special Publication 99,

622   pp. 83-109.

623 Rebesco, M., Hernández-Molina, F.J., van Rooij, D., Wåhlin, A., 2014. Contourites and

624   associates sediments controlled by deep-water circulation processes: State of the art

625   and future considerations. Marine Geology 352, 111-154.

626 Reijenstein, H.M., Posamentier, H.W., Bhattacharya, J.P., 2011. Seismic geomorphology and

627   high-resolution seismic stratigraphy of inner-shelf fluvial, estuarine, deltaic, and

628   marine sequences, Gulf of Thailand. AAPG Bulletin 95, 1959-1990.

629 Rijks, E.J.H., Jauffred, J.C.E.M., 1991. Seismic interpretation 29; attribute extraction; an

630   important application in any detailed 3-D interpretation study. The Leading Edge 10,

631   11-19.

632 Reynolds, D.J., Steckler, M.S., Coakley, B.J., 1991. The role of the sediment load in

633   sequence stratigraphy: The influence of flexural isostasy and compaction. Journal of

634   Geophysical Research B01914.

635 Sinclair, H.D., Tomasso, M., 2002. Depositional Evolution of Confined Turbidite Basins.

636   Journal of Sedimentary Research 72, 451-456.

637 Smith, R., 2004. Silled sub-basins to connected tortuous corridors: sediment distribution

638   systems on topographically complex sub-aqueous slopes. Geological Society of

639   London Special Publications 222, 23-43.

640 Smith, D.P., Kvitek, R., Iampietro, P.J., Wong, K., 2007. Twenty-nine months of geomorphic

641   change in upper Monterey Canyon (2002–2005). Marine Geology 236, 79-94.

642 Soutter, E.L., Kane, I.A., Huuse, M., 2018. Giant submarine landslide triggered by Paleocene

643   mantle plume activity in the North Atlantic. Geology 46, 511-514.

644 Symons, W.O., Sumner, E.J., Talling, P.J., Cartigny, M.J.B., Clare, M.A., 2016. Large-scale

645 sediment waves and scours on the modern seafloor and their implications for the

646 prevalence of supercritical flows. Marine Geology 371, 130-148.

647 Talling, P.J., Allin, J., Armitage, D.A., Arnott, R.W.C., Cartigny, M.J.B., Clare, M.A.,

648 Felletti, F., Covault, J.A., Girardclos, S., Hansen, E., Hill, P.R., Hiscott, R.N., Hogg,

649 A.J., Hughes Clarke, J.E., Jobe, Z.R., Malgesini, G., Mozzato, A., Naruse, H.,

650 Parkinson, S., Peel, F.J., Piper, D.J.W., Pop, E., Postma, G., Rowley, P., Sguazzini, A.,

651 Stevenson, C.J., Sumner, E.J., Sylvester, Z., Watts, C., Xu, J., 2015. Key future

652 directions for research on turbidity currents and their deposits. Journal Sedimentary

653 Research 85, 153-169.

654 Vail, PR., 1987. Seismic stratigraphy interpretation using sequence stratigraphy. Part I:

655 Seismic stratigraphy interpretation procedure. In Atlas of Seismic Stratigraphy, ed.

656 AW Bally, pp. 1-10. Am. Assoc. Petrol. Geol. Stud. Geol. No. 27, Vol. 1. 125 pp.

657 Winker, C.D., 1996. High-resolution seismic stratigraphy of a late Pleistocene submarine fan

658 ponded by salt-withdrawal mini-basins on the Gulf of Mexico continental slope. 28th

659 Annual Offshore Technology Conference, Proceedings, pp. 619-628.

660 Wynn, R.B., Stow, D.A.V., 2002. Classification and characterisation of deep-water sediment

661 waves. Marine Geology 192, 7-22.
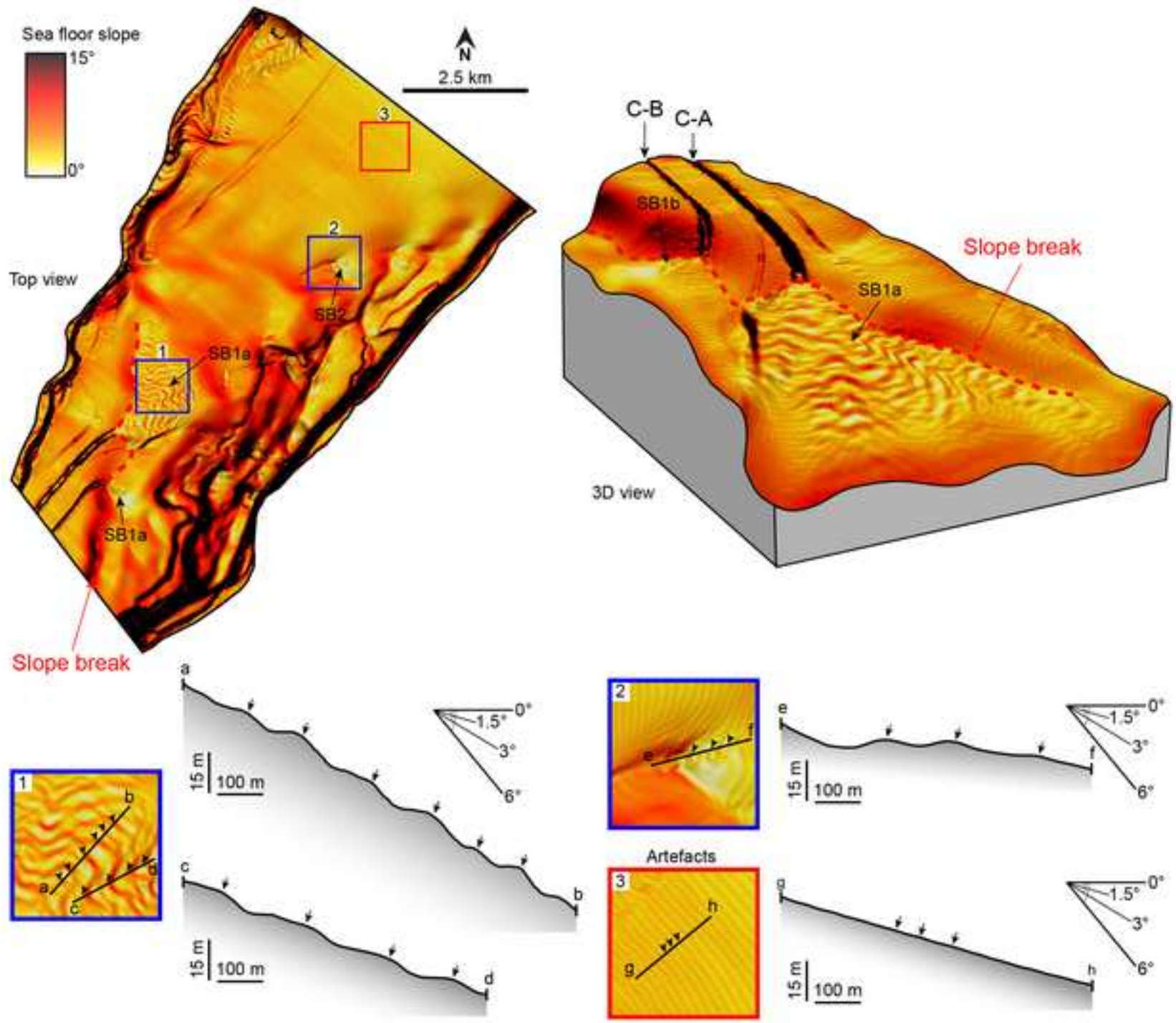
Figure 2

Figure 3

Sea floor Variance - 3D view
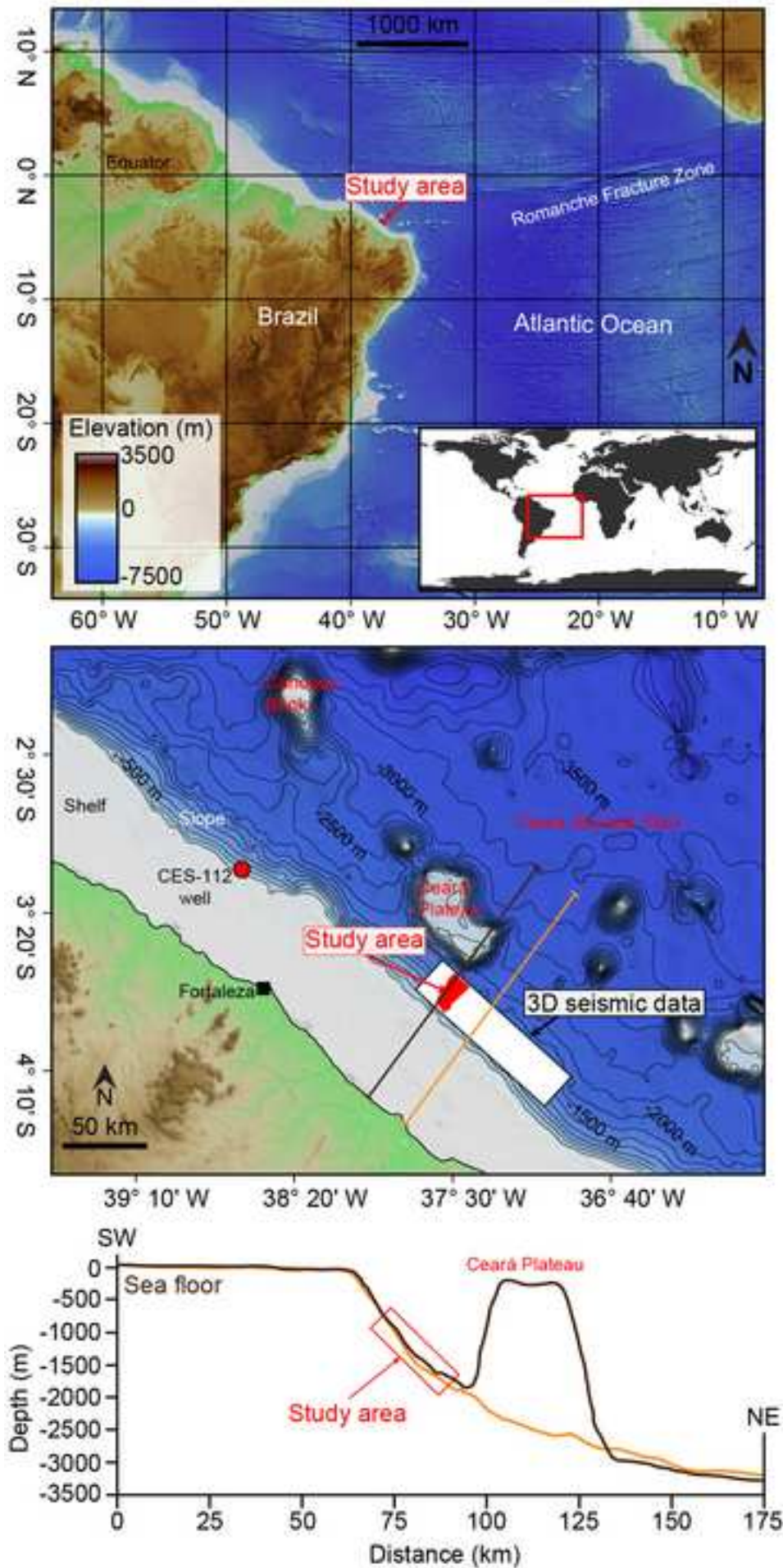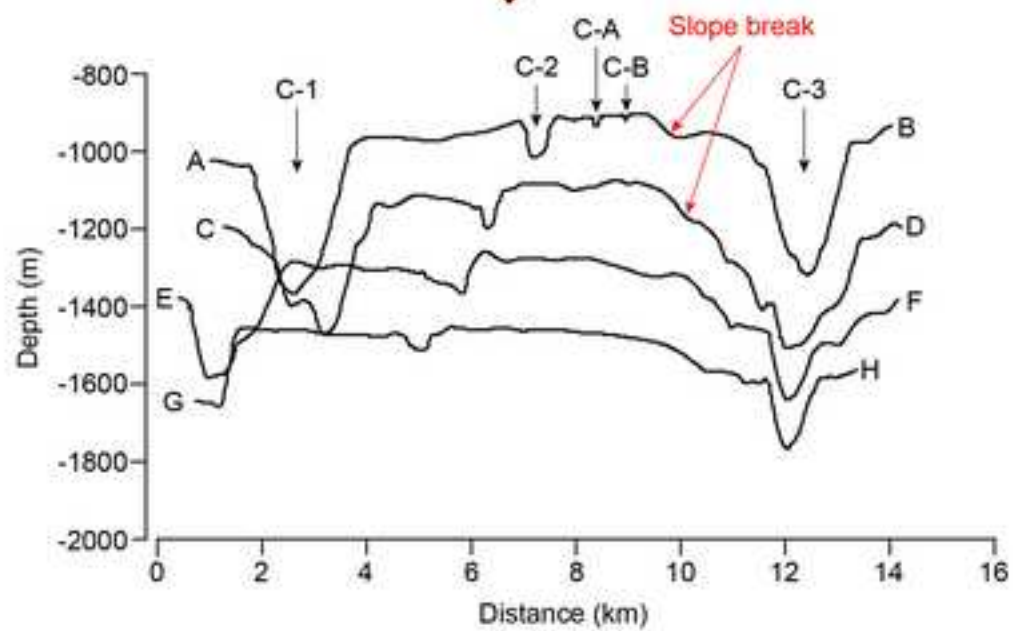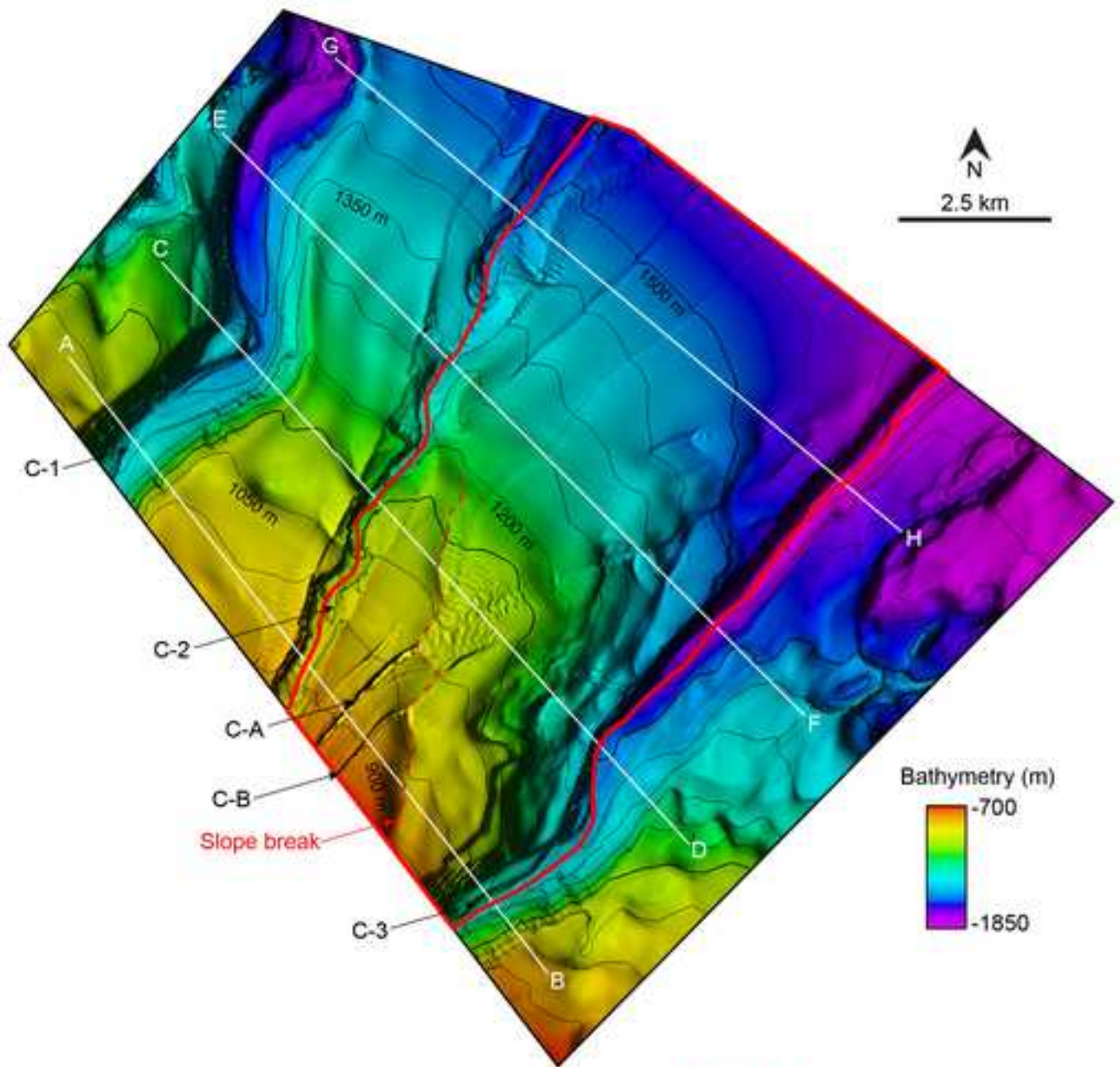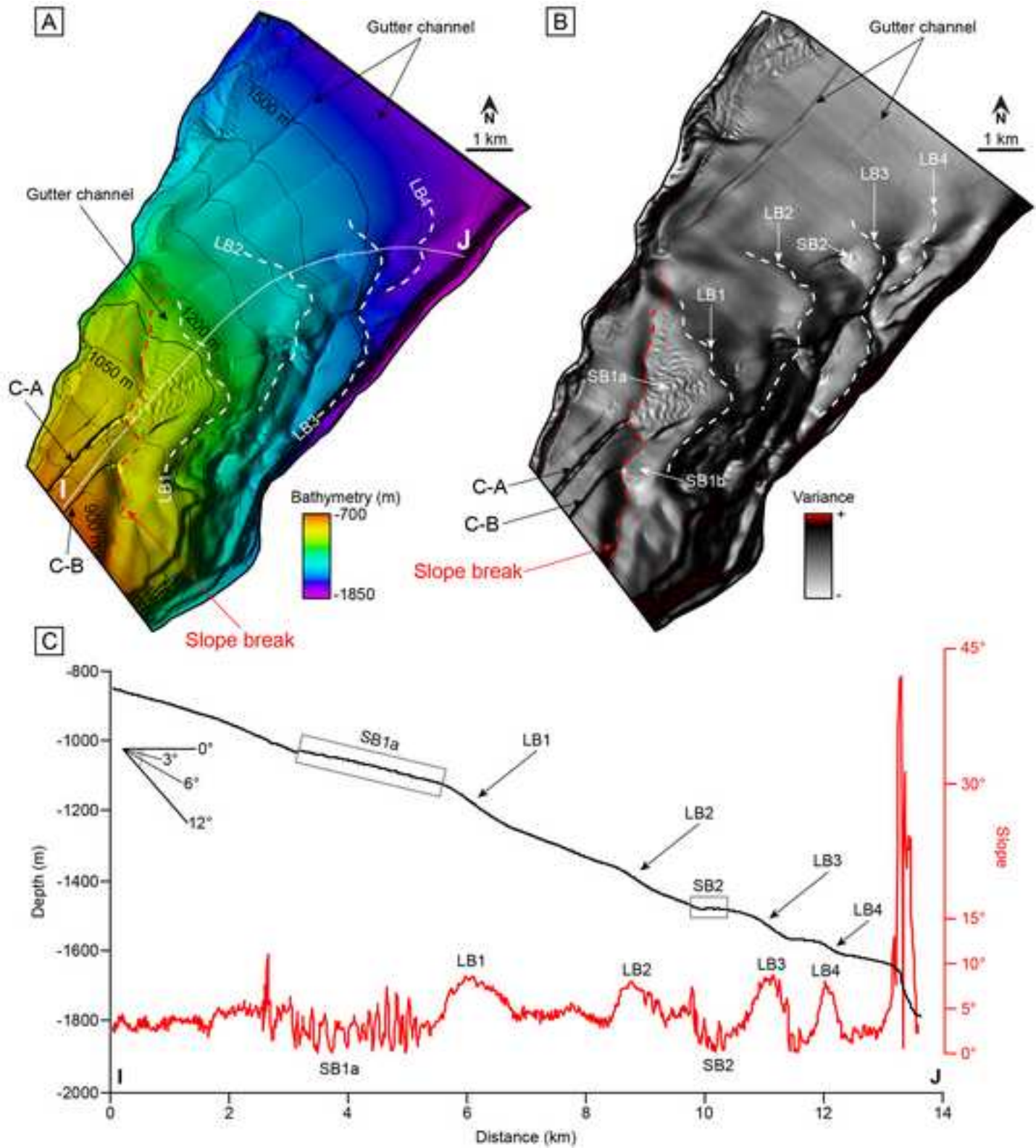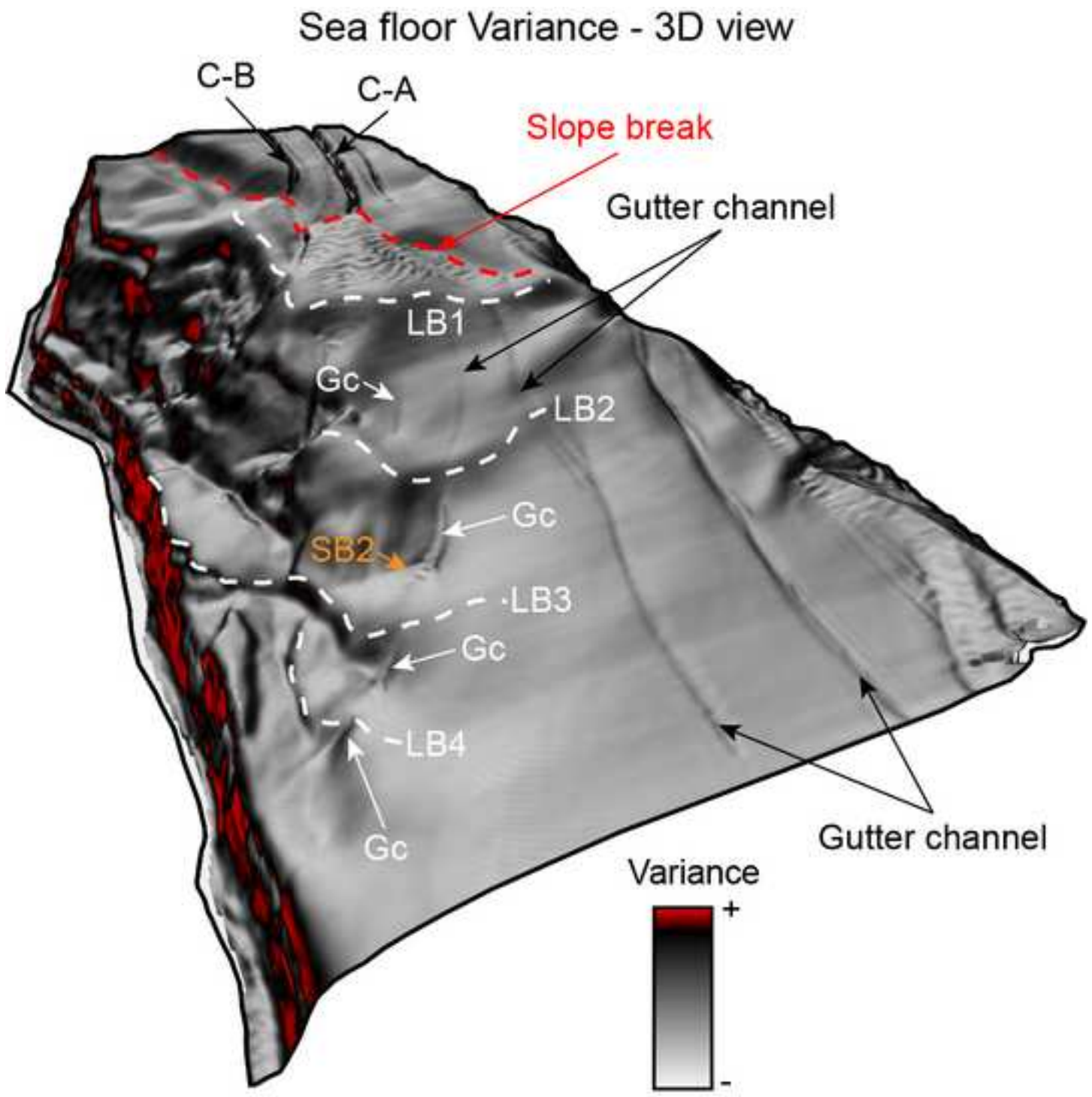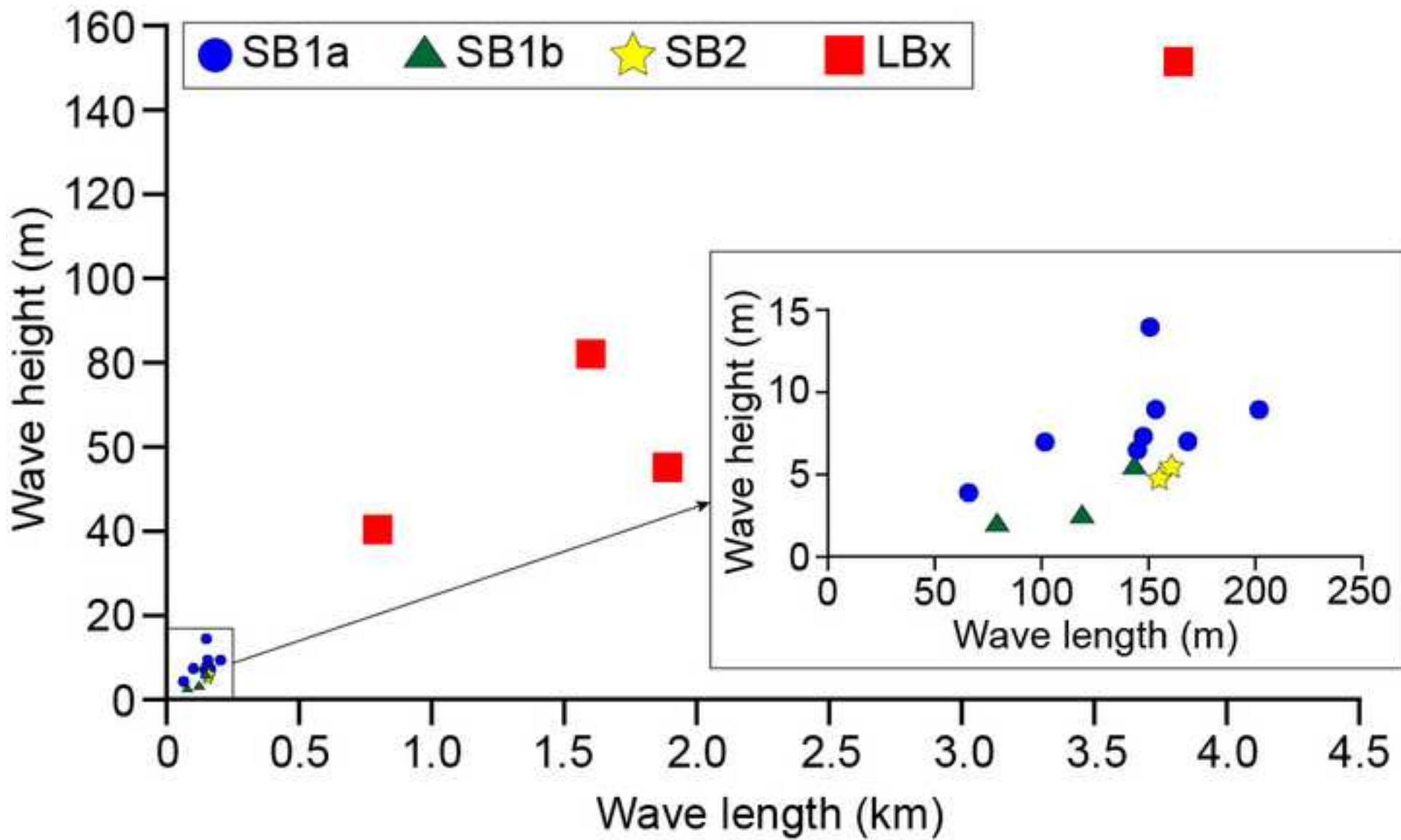
Figure 5

Figure 6
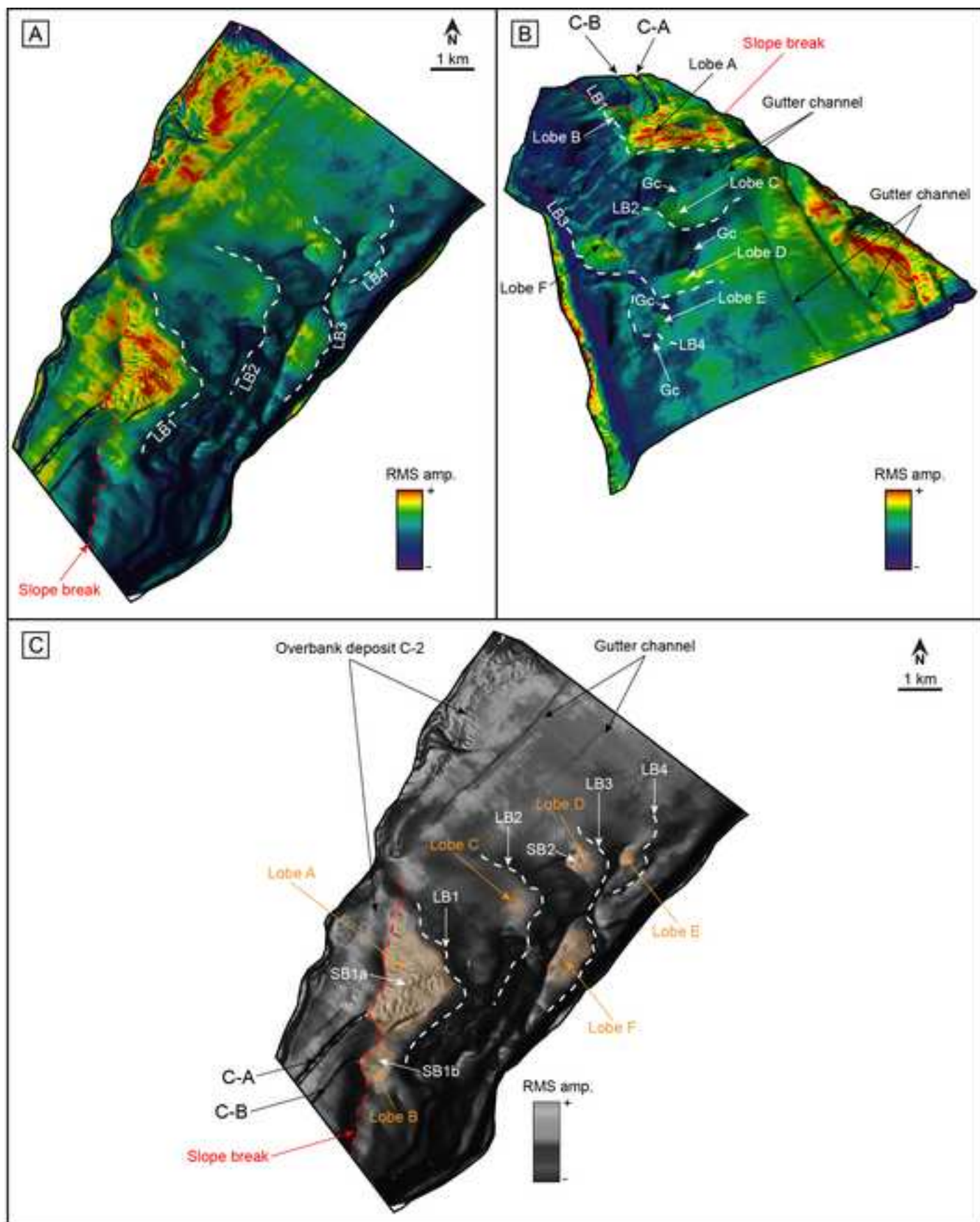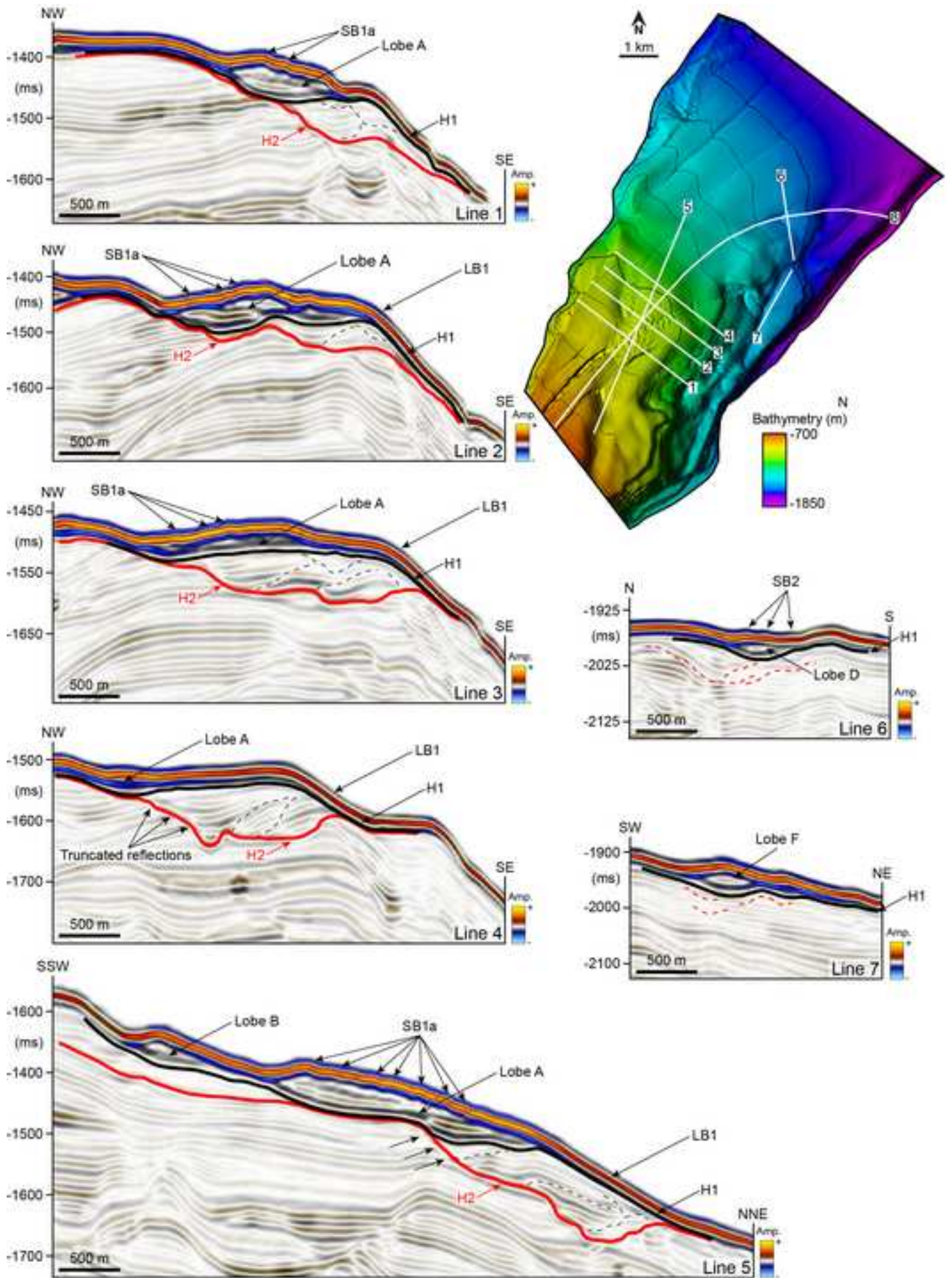**Click here to download high resolution image**

Figure 8
[Click here to download high resolution image](#)

Figure 9